



2 DOCTORAL THESIS

4 Optimisation studies and background
5 estimation in searches for the supersymmetric
6 partner of the top quark in all-hadronic final
7 states with the ATLAS Detector at the LHC

9 *A thesis submitted in fulfillment of the requirements
10 for the degree of Doctor of Philosophy*

11 *in the*

12 Experimental Particle Physics Research Group
13 School of Mathematical and Physical Sciences

14 *Author:*
15 Fabrizio MIANO

Supervisor:
Dr. Fabrizio SALVATORE

11th October 2017

Dedicated to my family.

*Have no fear for atomic energy
'cause none of them can stop the
time*

17

Robert Nesta Marley

18

Acknowledgments

19 Thanks to every single thing that went wrong. It made me stronger.

20

Declaration

22 I, Fabrizio MIANO, hereby declare that this thesis, titled, "Optimisation studies and back-
23 ground estimation in searches for the supersymmetric partner of the top quark in all-
24 hadronic final states with the ATLAS Detector at the LHC" has not been and will not be,
25 submitted in whole or in part to another University for the award of any other degree.

26 *Brighton, June 2018*

University of Sussex
School of Mathematical and Physical Sciences
Experimental Particle Physics Research Group

Doctoral Thesis

33 Optimisation studies and background estimation in searches for
34 the supersymmetric partner of the top quark in all-hadronic final
35 states with the ATLAS Detector at the LHC

37 by Fabrizio Miano

Abstract

This thesis presents searches for supersymmetry in $\sqrt{s} = 13$ TeV proton-proton collisions at the LHC using data collected by the ATLAS detector in 2015, 2016 and 2017. Events with 4 or more jets and missing transverse energy were selected. Kinematic variables were investigated and optimisations were performed to increase the sensitivity to supersymmetric signals. Standard Model backgrounds were estimated by means of Monte Carlo simulations and data-driven techniques. Before analysing the data in the blinded signal regions the agreement between data and background predictions and the extrapolations from control and validation regions to signal regions were validated. The analysis yielded no significant excess in any of the analyses performed. Therefore limits were set and the results were interpreted as lower bounds on the masses of supersymmetric particles in various scenarios and models.

⁵⁰ Contents

⁵¹	Introduction	1
⁵²	1 The Standard Model, Supersymmetry, and the motivations behind it	2
⁵³	1.1 The Standard Model	2
⁵⁴	1.1.1 Overview	3
⁵⁵	1.1.2 Limitations of the Standard Model	4
⁵⁶	1.2 Supersymmetry	4
⁵⁷	1.2.1 Why SUSY?	4
⁵⁸	1.2.2 Minimal Supersymmetric Standard Model	4
⁵⁹	1.2.3 <i>R</i> -parity SUSY	4
⁶⁰	1.2.4 Simplified models	4
⁶¹	1.2.5 Phenomenological MSSM	4
⁶²	2 The ATLAS Experiment at the LHC	5
⁶³	2.1 The LHC	5
⁶⁴	2.2 The ATLAS Detector	8
⁶⁵	2.2.1 The Magnet System	9
⁶⁶	2.2.2 The Inner Detector	10
⁶⁷	2.2.3 The Calorimeters	13
⁶⁸	2.2.4 The Muon Spectrometer	15
⁶⁹	2.3 The ATLAS Trigger System	16
⁷⁰	2.3.1 Level 1 Trigger	17
⁷¹	2.3.2 High-Level Trigger	18
⁷²	3 The <i>b</i>-jet Trigger Signature in ATLAS	19
⁷³	3.1 Trigger Efficiency	19

74	4 Event Simulation and Reconstruction	20
75	4.1 Event Generation	21
76	4.1.1 Parton Distribution Functions (PDFs)	21
77	4.1.2 Matrix Element Calculation	21
78	4.1.3 Parton Showers	21
79	4.1.4 Hadronisation	21
80	4.2 Detector Simulation	21
81	4.3 Reconstruction	21
82	4.3.1 Pile-up in the Inner Detector	21
83	4.3.2 Tracks	21
84	4.3.3 Vertex	21
85	4.3.4 Electrons	21
86	4.3.5 Muons	21
87	4.3.6 Jets	21
88	4.3.7 Taus	21
89	4.3.8 Missing Transverse Energy	21
90	4.4 Object Selection	21
91	4.4.1 Baseline Leptons	21
92	4.4.2 Baseline Jets	21
93	4.4.3 Baseline Taus	21
94	4.4.4 Overlap Removal	21
95	4.4.5 Signal Leptons	21
96	4.4.6 Signal Jets	21
97	4.4.7 Signal Taus	21
98	4.5 Monte Carlo Samples	21
99	4.5.1 Generators	21
100	4.5.2 SM Background MC Samples	21
101	4.5.3 MC Signal Sample	21
102	5 Stop Searches in all-hadronic final states	22
103	6 Results and Statistical Interpretations	23
104	A Appendix A	24
105	B Appendix B	25

¹⁰⁷ **List of Tables**

¹⁰⁸ List of Figures

¹⁰⁹ 2.1	CERN Accelerator complex. The LHC is the last ring (dark grey line). Smaller machines are used for early-stage acceleration and also to provide beams for other experiments [1].	7
¹¹⁰ 2.2	Cut-away view of the ATLAS detector. The dimensions of the detector are 25 m in height and 44 m in length. The overall weight of the detector is approximately 7000 tonnes [1].	8
¹¹¹ 2.3	The ATLAS magnet system.	10
¹¹² 2.4	The ATLAS Inner Detector	11
¹¹³ 2.5	A computer generated image of the full calorimeter.	13
¹¹⁴ 2.6	Cut-away view of the ATLAS muon system [2].	15
¹¹⁵ 2.7	The ATLAS TDAQ system. L1Topo and FTK were being commissioned during 2015 and not used for the results shown in this thesis [3].	16
¹¹⁶		
¹¹⁷		
¹¹⁸		
¹¹⁹		
¹²⁰		

¹²¹ Introduction

¹²² Last thing to write

¹²³ **Chapter 1**

¹²⁴ **The Standard Model,
Supersymmetry, and the motivations
behind it**

¹²⁷ *A theory is something nobody believes, except the person who made it. An experiment is something everybody believes, except the person who made it.*

Albert Einstein

¹²⁸ The Standard Model (SM) of particle physics is an effective theory that aims to provide
¹²⁹ a general description of fundamental particles and the phenomena we see in nature, i. e.
¹³⁰ the way they interact. Unfortunately, our understanding of nature is still limited due to
¹³¹ some opened question to which the SM is not able to answer to, yet.

¹³² In this chapter, an overview of the SM will be presented in Section 1.1 together with
¹³³ the limitations of such theory and some of the reasons behind the need of an extension.
¹³⁴ For the last decades theoretical physicsts have been trying to provide extensions to the
¹³⁵ SM, the so-called beyond-the-SM theories. Among these, one of the most popular, Super-
¹³⁶ symmetry which will be discussed in Section 1.2.

¹³⁷ **1.1 The Standard Model**

¹³⁸ The 20th century can be considered a quantum revolution. Several experiments led to
¹³⁹ discoveries which were found to be, together with the formalised theory, a solid base of

¹⁴⁰ the Standard Model of particle physics and our description of nature. Several particles
¹⁴¹ were predicted first by the SM and then experimentally observed e.g. the W and the Z
¹⁴² bosons, the τ lepton, [4], and more recently the Higgs boson at the LHC discovered by
¹⁴³ ATLAS [5] and CMS [6].

¹⁴⁴ The SM lays on a Quantum Field Theory (QFT) where particles are treated like fields.
¹⁴⁵ It can describe three of the four fundamental forces; weak, electromagnetic, and strong.
¹⁴⁶ As of today, gravity is not considered in the SM. Sections 1.1.1 and 1.1.2 will be focused
¹⁴⁷ on the description of the fields together with the carriers of the information, and on the
¹⁴⁸ limitations that such theory implies, respectively.

¹⁴⁹ 1.1.1 Overview

¹⁵⁰ The most general classification of the particles within the SM can be made by means of
¹⁵¹ spin. Fermions have half-integer spin values - and are usually referred to as matter -, and
¹⁵² bosons have integer-spin values. A noteworthy subset of bosons is formed by the Spin-1
¹⁵³ bosons (also known as gauge bosons). These can be considered the information carriers
¹⁵⁴ or, in fact, the mediators of the forces.

¹⁵⁵ Fermions

¹⁵⁶ Six quarks and six leptons belong to the fermions family. The six quarks of the SM can
¹⁵⁷ be grouped into three doublets. The up-type quarks (up, charm, top) have charge $+\frac{2}{3}e$
¹⁵⁸ and the down-type quarks (down, strange, beauty/bottom) have charge $-\frac{1}{3}e$, where e is
¹⁵⁹ the electron charge. Quarks also have another quantum number that can be seen as the
¹⁶⁰ analogue of the electric charge, the colour charge. There are three different states of the
¹⁶¹ colour charge; "red", "green" and "blue".

$$\begin{pmatrix} u \\ d \end{pmatrix}, \quad \begin{pmatrix} c \\ s \end{pmatrix}, \quad \begin{pmatrix} t \\ b \end{pmatrix}$$

¹⁶² Three of the six leptons (electron e , muon μ , tau τ) are electrically charged and three
¹⁶³ of them electrically neutral (electron neutrino ν_e , muon neutrino ν_μ , tau neutrino ν_τ). When
¹⁶⁴ referring to fermions they can also be grouped into generations. Fermions are also grouped
¹⁶⁵ in generations. Each generation contains four particles; one charged lepton, one neut-
¹⁶⁶ rino, and one up- and down-type quark. The masses of the charged leptons and quarks
¹⁶⁷ increase with the generation.

$$\begin{pmatrix} \nu_e \\ e^- \end{pmatrix}, \quad \begin{pmatrix} \nu_\mu \\ \mu^- \end{pmatrix}, \quad \begin{pmatrix} \nu_\tau \\ \tau^- \end{pmatrix}$$

₁₆₈ **Forces of Nature**

₁₆₉ **1.1.2 Limitations of the Standard Model**

₁₇₀ **1.2 Supersymmetry**

₁₇₁ **1.2.1 Why SUSY?**

₁₇₂ **1.2.2 Minimal Supersymmetric Standard Model**

₁₇₃ **1.2.3 R-parity SUSY**

₁₇₄ **1.2.4 Simplified models**

₁₇₅ **1.2.5 Phenomenological MSSM**

¹⁷⁶ **Chapter 2**

¹⁷⁷ **The ATLAS Experiment at the LHC**

¹⁷⁸ ATLAS (A Toroidal LHC ApparatuS) is one of the four main experiments (ATLAS, CMS,
¹⁷⁹ ALICE, LHCb) taking data at a center-of-mass energy of 13 TeV using beams delivered by
¹⁸⁰ the Large Hadron Collider (LHC). In this chapter an overview of the LHC will be given
¹⁸¹ in Section 2.1, then the ATLAS detector will be described in Section 2.2, and finally the
¹⁸² Trigger system, used to cleverly store the data, will be described in Section 2.3. A more
¹⁸³ in-depth description of the Trigger algorithms I have been involved in will be given in
¹⁸⁴ Chapter 3.

¹⁸⁵ **2.1 The LHC**

¹⁸⁶ As of today, the LHC is the worlds largest and most powerful particle accelerator. It
¹⁸⁷ was designed to help answer some of the fundamental open questions in particle phys-
¹⁸⁸ ics by colliding protons at an unprecedeted energy and luminosity. It is located at the
¹⁸⁹ European Organisation for Nuclear Research (CERN), in the Geneva area, at a depth ran-
¹⁹⁰ ging from 50 to 175 metres underground. It consists of a 27-kilometre ring made of su-
¹⁹¹ perconducting magnets, and inside it two high-energy particle beams travel in opposite
¹⁹² directions and in separate beam pipes.

¹⁹³ The beams are guided around the ring by a strong magnetic field generated by coils -
¹⁹⁴ made of special electric cables - that can operate in a superconducting regime. 1232 super-
¹⁹⁵ conducting dipole and 392 quadrupole magnets, with an average magnetic field of 8.3 T,
¹⁹⁶ are employed and kept at a temperature below 1.7 K, in order to preserve their supercon-
¹⁹⁷ ducting properties. The formers are used to bend the beams and the latters to keep them
¹⁹⁸ focused while they get accelerated.

¹⁹⁹ The collider first went live on September 2008 even though, due to a magnet quench

200 incident that damaged over 50 superconducting magnets, it has been operational since
 201 November 2009 when low-energy beams circulated in the tunnel for the first time since
 202 the incident. This also marked the start of the main research programme and the begin-
 203 ning of the so-called Run 1: first operational run (2009 - 2013).

204 Performance of the LHC

205 In June 2015 the LHC restarted delivering physics data, after a two-year break, the so-
 206 called Long Shutdown 1 (LS1), during which the magnets were upgraded to handle the
 207 current required to circulate 7-TeV beams. It was the beginning of the so-called Run 2 -
 208 second operational run (2015-2018) - during which LHC has collided up to 10^{11} bunches
 209 of protons every 25 ns at the design luminosity - the highest luminosity the detector was
 210 designed to cope with - of $2 \cdot 10^{34} \text{ cm}^{-2} \text{s}^{-1}$. The definition of the luminosity is:

$$\mathcal{L} = f \frac{n_b N_1 N_2}{4\pi\sigma_x\sigma_y} \quad (2.1)$$

211 where N_1 and N_2 are the number of protons per bunch in each of the colliding beams, f
 212 is the revolution frequency of the bunch collisions, n_b the number of proton per bunch,
 213 and σ_x and σ_y are the horizontal and vertical dimensions of the beam. The luminosity is
 214 strictly related to the number of collisions occurring during a certain experiment via the
 215 following:

$$\mathcal{N}_{\text{event}} = \mathcal{L}\sigma_{\text{event}} \quad (2.2)$$

216 where σ_{event} is the cross section of the process under investigation. It has not only collided
 217 protons but also heavy ions, in particular lead nuclei at $\sqrt{s_{NN}} = 5.02 \text{ TeV}$, at a luminosity
 218 of $10^{27} \text{ cm}^{-2} \text{s}^{-1}$ [7].

219 Acceleration stages

220 Before reaching the maximum energy, the proton beams are accelerated by smaller ac-
 221 celerators through various stages. Figure 2.1 shows a sketch of the CERN's accelerator
 222 complex. It all begins at the linear accelerator LINAC 2. Here protons are accelerated up
 223 to 50 MeV, and then injected in the Proton Synchrotron Booster (PSB) where they reach
 224 1.4 GeV. The next stage is the Proton Synchrotron (PS), which boosts the beams up to 25
 225 GeV and then the Super Proton Synchrotron (SPS) makes them reach energies up to 450
 226 GeV. Eventually, the beams are injected in bunches with a 25 ns spacing into the LHC,
 227 where they travel in opposite directions, while they are accelerated to up to 13 TeV. Once

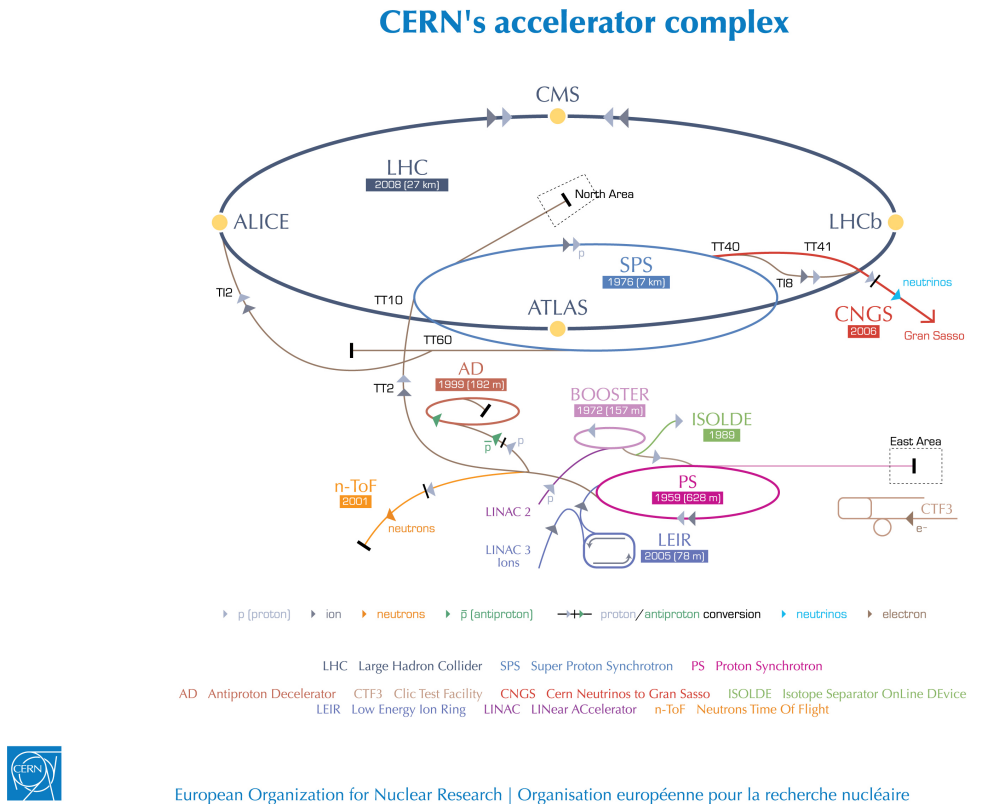


Figure 2.1: CERN Accelerator complex. The LHC is the last ring (dark grey line). Smaller machines are used for early-stage acceleration and also to provide beams for other experiments [1].

- 228 the bunches reach the maximum energy, they are made collide at four different points,
 229 inside four experiments around the ring [8].

230 The heavy ion beams acceleration procedure is slightly different. Their journey starts
 231 at LINAC 3 first, and the Low Energy Ion Ring (LEIR) then, before they make their way
 232 into the PS where they follow the same path as the protons [8].

233 The four large detectors on the collision points are; the multi-purpose detectors A Tor-
 234 oidal LHC ApparatuS (ATLAS), and Compact Muon Solenoid (CMS) [9], Large Hadron
 235 Collider beauty (LHCb) [10], which focuses on flavour physics, and A Large Ion Collider
 236 Experiment (ALICE) [11] which specialises in heavy ion physics. The *big four* are not the
 237 only experiments at the CERN's accelerator complex. There also are smaller experiments
 238 based at the the four caverns about the collision points e.g. TOTEM, LHCf and MoEDAL,
 239 but this will not be discussed any further in this thesis.

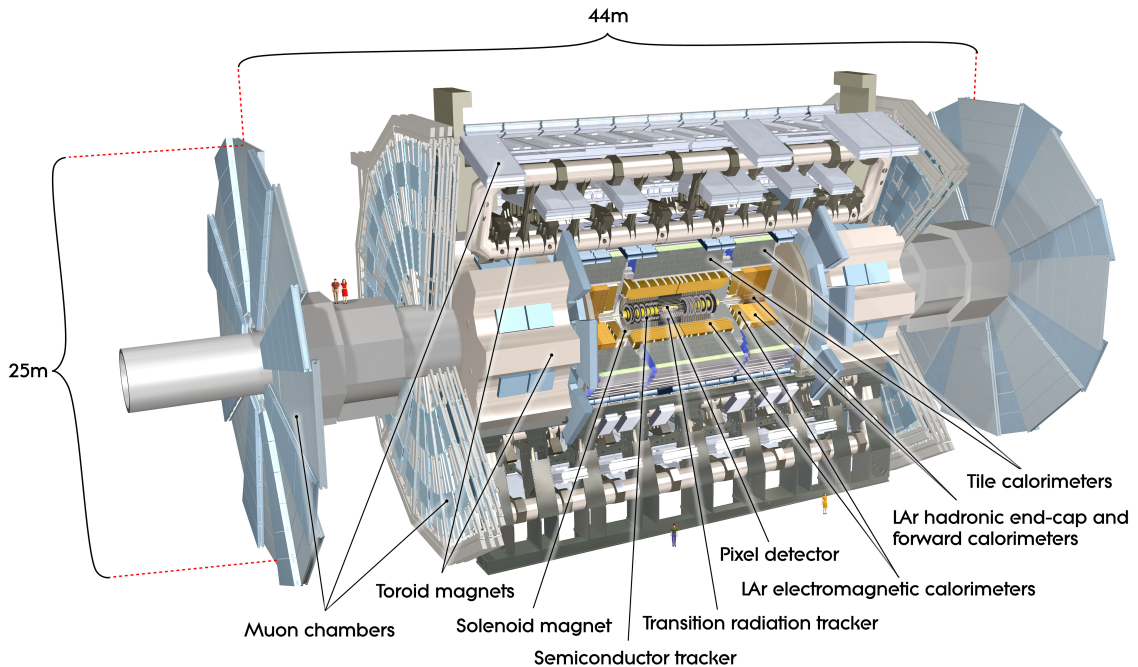


Figure 2.2: Cut-away view of the ATLAS detector. The dimensions of the detector are 25 m in height and 44 m in length. The overall weight of the detector is approximately 7000 tonnes [1].

²⁴⁰ 2.2 The ATLAS Detector

²⁴¹ ATLAS is a general-purpose detector designed to collect data with the highest luminosity
²⁴² provided by the LHC. It is located at CERN’s Point 1 cavern and it measures about 45 m in
²⁴³ length and 25 m in diameter. It has a forward-backward symmetric cylindrical geometry
²⁴⁴ with respect to the interaction point and it is designed to reconstruct and measure physics
²⁴⁵ objects such as electrons, muons, photons and hadronic jets. Its design was optimised to
²⁴⁶ be as sensitive as possible to the discovery of the Higgs boson and beyond-the-Standard-
²⁴⁷ Model (BSM) physics. In fact, thanks to the other sub-systems, ATLAS is able to observe
²⁴⁸ all possible decay products by covering nearly 4π steradians of solid angle.

²⁴⁹ In Figure 2.2 a cut-away view of ATLAS with all its components is shown. The inner-
²⁵⁰ most layer is the Inner Detector (ID) which is the core of the tracking system and consists
²⁵¹ of a Pixel, a Silicon micro-strip tracker (SCT), and a Transition Radiation Tracker (TRT).
²⁵² It is submerged in a 2 T magnetic field, generated by a thin superconducting solenoid,
²⁵³ which bends all the charged particles’ trajectories allowing transverse momentum meas-
²⁵⁴ urement. The electromagnetic and hadronic calorimeters form the next layer and they are
²⁵⁵ both used to perform precise energy measurements of photons, electrons, and hadronic

256 jets. Finally, the outermost layer corresponds to the Muon Spectrometer (MS) which, to-
257 gether with the ID, enclosed in a toroidal magnetic field, allows precise measurement of
258 momentum and position of muons. These sub-detectors will be discussed in more detail
259 in the following sections.

260 The ATLAS coordinate system

261 A coordinate system is taken on for the spatial definition of the sub-systems and kin-
262 ematic measurement of physics processes. Such system is defined starting from the in-
263 teraction point, defined as the origin. The z -axis is defined by the beam direction and the
264 $x - y$ plan, as transverse to the beam direction.

265 A quantity, known as pseudorapidity, (η), is defined to describe the angle of a particle
266 coming out of the collision, with respect to the beam axis:

$$\eta \equiv -\ln(\tan(\theta/2))$$

267 Here θ is the polar angle. The azimuthal angle, ϕ , is defined around the beam axis and
268 the polar angle. In the (η, ϕ) space a distance ΔR can be therefore defined as

$$\Delta R = \sqrt{\Delta\eta^2 + \Delta\phi^2}$$

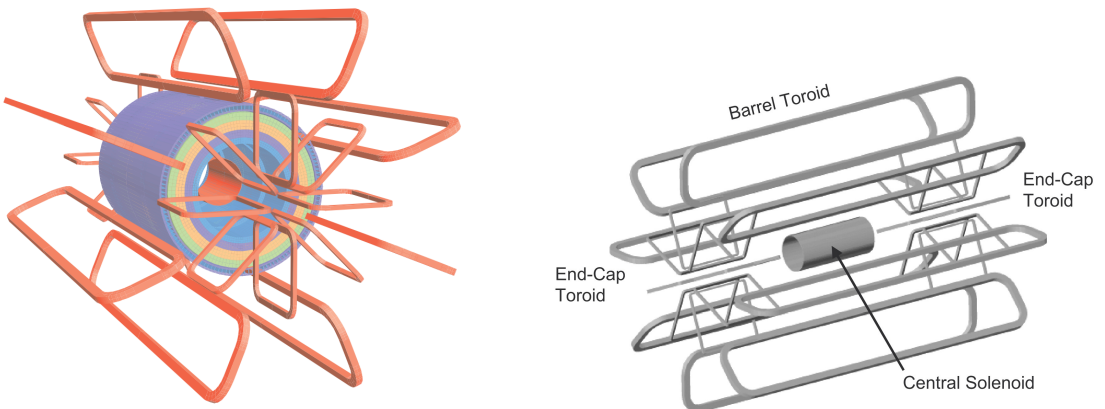
269 where $\Delta\eta$ and $\Delta\phi$ are the differences in pseudorapidity and azimuthal angle between
270 any two considered objects. A central and a forward region of pseudorapidity are also
271 defined such that the detector components are described as part of the *barrel* if they belong
272 to the former or as part of the *end-caps* if they belong to the latter.

273 2.2.1 The Magnet System

274 The ATLAS magnet system, 26 m long with a 22 m diameter, generates the magnetic
275 field needed to bend the trajectories of charged particles in order to perform momentum
276 measurement. Figure 2.3a and 2.3b show the geometry of the system and its compo-
277 nents, which are made of NbTi - superconducting material - and will be described in the
278 following paragraphs.

279 The Central Solenoid

280 With an axial length of 5.8 m, an inner radius of 2.46 m, and an outer radius of 2.56 m, the
281 central solenoid magnet is located between the ID and the ECAL. Its function is to bend



(a) Geometry of magnet windings and tile calorimeter steel. The eight barrel toroid coils, with the end-cap coils interleaved are visible. The solenoid winding lies inside the calorimeter volume [2].

(b) Schematic view of the superconducting magnets [12].

Figure 2.3: The ATLAS magnet system.

282 the charged particles that go through the ID and it is aligned on the beam axis providing
 283 a 2 T axial magnetic field that allows accurate momentum measurement up to 100 GeV
 284 [12].

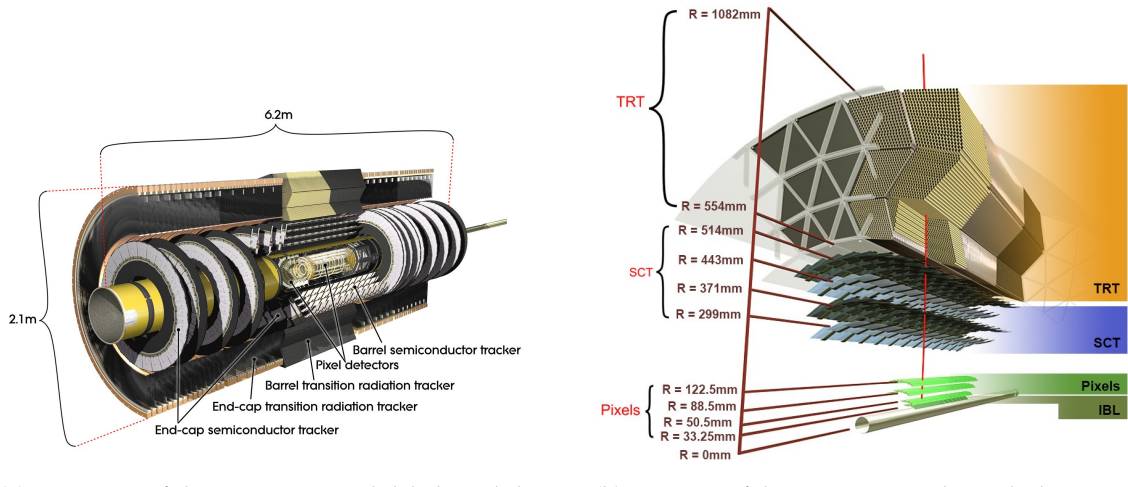
285 The Barrel and the End-cap Toroids

286 Figure 2.3b displays the toroid magnetic system that surrounds the calorimeters. With
 287 its cylindrical shape this component consists of a barrel and two end-caps toroids, each
 288 with eight superconducting coils. The system allows accurate measurement of muon
 289 momenta using a magnetic field of approximately 0.5 T (barrel) for the central regions
 290 and 1 T (end-cap) for the end-cap regions, respectively, which bends the particles in the
 291 θ direction.

292 2.2.2 The Inner Detector

293 The Inner Detector (ID) [13] is the innermost component of the ATLAS detector i. e. the
 294 nearest sub-detector to the interaction region and it is used to reconstruct charged particle
 295 tracks used in the selection of physics objects. In fact, it allows robust track reconstruc-
 296 tion, with accurate impact parameter resolution ($\sim 20\mu m$) and precise primary and sec-
 297 ondary vertex reconstruction for charged particles (tracks) above 500 MeV and within
 298 $|\eta| < 2.5$.

299 The ID is comprised of independent and concentric sub-systems, which are all shown



(a) Overview of the ATLAS ID with labels and dimensions.

(b) Diagram of the ATLAS ID and its sub-detectors.

Figure 2.4: The ATLAS Inner Detector

300 in Figure 2.4:

301 • Insertable B-Layer (IBL):

302 innermost Pixel Detector layer added during ATLAS Run-2 upgrade (2013/2014)
303 to improve vertexing and impact parameter reconstruction;

304 • Silicon Pixel Tracker (Pixel):

305 made of silicon pixel layers and used mainly for reconstructing both the primary
306 and secondary vertices in an event;

307 • SemiConductor Tracker (SCT):

308 comprised of silicon microstrip layers; thanks to its resolution ($17 \times 580 \mu\text{m}$) it can
309 accurately measure particle momenta;

310 • Transition Radiation Tracker (TRT):

311 final layer comprised of various layers of gaseous straw tube elements surrounded
312 by transition radiation material.

313 These sub-detectors will be discussed in the following sections.

314 **IBL**

315 The IBL [14] is the innermost Pixel Detector layer as shown in Figure 2.4b. It is comprised
316 of 6M channels and each pixel measures $50 \times 250 \mu\text{m}$. Its resolution is $8 \times 40 \mu\text{m}$,
317 The addition of this new layer brought a considerable improvement on the performance of the

³¹⁸ Pixel Detector by enhancing the quality of impact parameter reconstruction of tracks. In
³¹⁹ particular, this was achieved by improving the vertex finding efficiency and the tagging
³²⁰ of bottom-quark-initiated jets (*b*-jets) which, in case of a B-layer failure, can be restored
³²¹ by the IBL. Besides these improvements, the IBL insertion allowed ATLAS to better cope
³²² with high luminosity effects such as the increase in event pile-up, which leads to high
³²³ occupancy and read-out inefficiency.

³²⁴ **Pixel**

³²⁵ The Pixel detector is comprised of 1750 identical sensorchip-hybrid modules, each cover-
³²⁶ ing an active area of 16.4×60.8 mm. The total number of modules correspond to roughly
³²⁷ 80 million semiconductor silicon pixels. The nominal pixel size is $50 \mu\text{m}$ in the ϕ direction
³²⁸ and $400 \mu\text{m}$ in the barrel region, along the z -axis (beam axis) [15]. The reason why such a
³²⁹ large amount of pixels is employed is justified by the need to cope with the high lumi-
³³⁰ nosity in ATLAS. The silicon pixel detector measures 48.4 cm in diameter and 6.2 m in length
³³¹ providing a pseudorapidity coverage of $|\eta| < 2.5$. Figure 2.4b shows the three concentric
³³² barrel layers placed at 50.5 mm, 88.5 mm and 122.5 mm respectively. Furthermore, the
³³³ Pixel detector is made of six disk layers, three for each forward region, such that when a
³³⁴ charged particle crosses the layers it will generate a signal at least in three space points.
³³⁵ The fine granularity of such detector allows accurate measurement and precise vertex
³³⁶ reconstruction, as it provides a more accurate position measurement as a large detection
³³⁷ area is available. In particular, it has a resolution of $10 \times 115 \mu\text{m}$.

³³⁸ **SCT**

³³⁹ The SCT is made of 4088 modules of silicon micro-strip detectors arranged in four con-
³⁴⁰ centric barrel layers. It is mainly used for precise momentum reconstruction over a range
³⁴¹ $|\eta| < 2.5$ and it was designed for precision measurement of the position using four points
³⁴² (corresponding to eight silicon layers), obtained as track hits when crossing the layers.
³⁴³ Figure 2.4b shows the structure of the SCT with its four concentric barrel layers with
³⁴⁴ radii ranging from 299 mm to 514 mm and two end-cap layers. Each module has an in-
³⁴⁵ trinsic resolution of $17 \mu\text{m}$ in the $R - \phi$ direction and $580 \mu\text{m}$ in the z direction. As the
³⁴⁶ SCT is further away from the beam-pipe than the Pixel detector, it has to cope with re-
³⁴⁷ duced particle density. This allows for reduced granularity maintaining the same level of
³⁴⁸ performance of the Pixel detector: SCT can use ~ 6.3 million read-out channels.

349 **TRT**

350 The last and outermost of the sub-systems in the ID is the TRT. It is a gaseous detector
351 which consists of 4 mm diameter straw tubes wound from a multilayer film reinforced
352 with carbon fibers and containing a 30 μm gold plated tungsten wire in the center. The
353 straw is filled with a gas mixture of 70% Xe, 27% CO₂ and 3% O₂ [16]. As shown in Fig-
354 ure 2.4b, its section consists of three concentric layers with radii ranging from 544 mm to
355 1082 mm, each of which has 32 modules containing approximately 50,000 straws, 1.44 m
356 in length, aligned parallel to the beam direction with independent read-out at both ends.
357 Both end-cap sections are divided into 14 wheels, with roughly 320,000 straws in the
358 R-direction. The average 36 hits per track in the central region of the TRT allow continu-
359 ous tracking to enhance pattern recognition and momentum resolution in the $|\eta| < 2.5$
360 region. It also improves the p_{T} resolution for longer tracks.

361 **2.2.3 The Calorimeters**

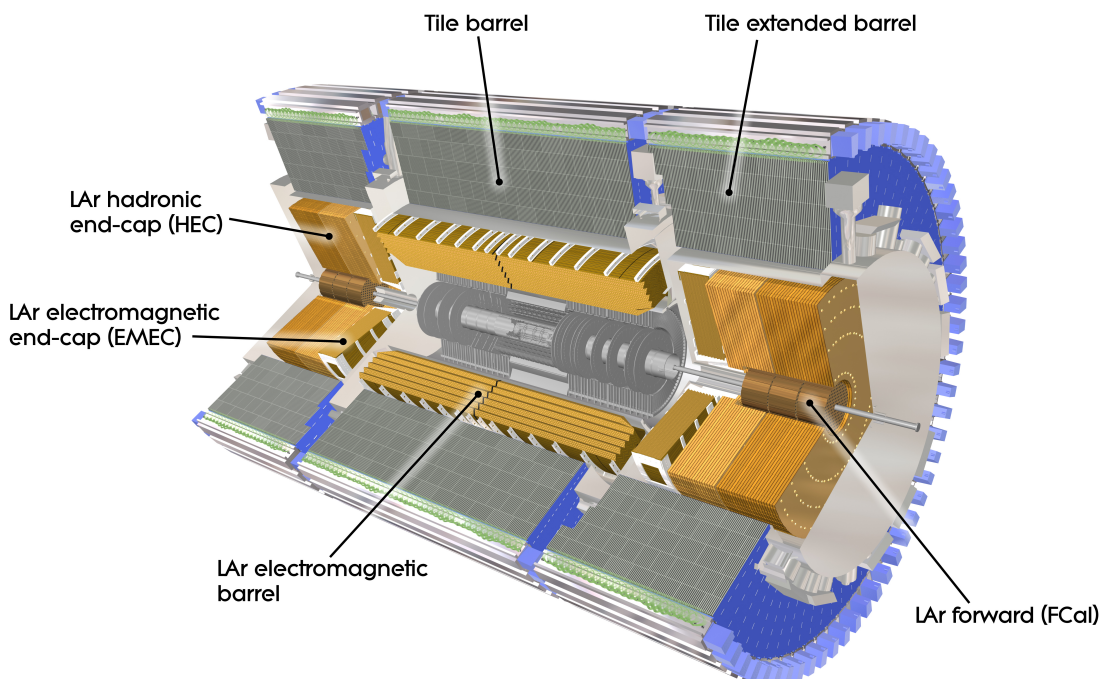


Figure 2.5: A computer generated image of the full calorimeter.

362 The ATLAS Calorimeter system, shown in Figure 2.5, is comprised of two main sub-
363 systems; the electromagnetic calorimeter (ECAL) and hadronic calorimeter (HCAL), which
364 are designed to stop and measure the energy of electromagnetic-interacting and had-

365 ronic particles respectively. The combination of the two provides full coverage in ϕ and
366 $|\eta| < 4.95$. Particles slow down and lose energy generating showers when crossing dif-
367 ferent layers.

368 The ECAL is comprised of one barrel and two end-cap sectors employing liquid Ar-
369 gon (LAr). The showers hereby develop as electrons pairs which are then collected.

370 The HCAL is also comprised of one barrel and two end-cap sectors. The sensors in
371 the barrel of the HCAL are tiles of scintillating plastic whereas LAr is employed for the
372 end-cap.

373 A forward region, the closest possible to the beam, is covered by a LAr forward calor-
374 imeter (FCal).

375 The LAr and Tile Calorimeter will be briefly discussed in the following parapgraphs.

376 The Liquid Argon Calorimeters

377 The ECAL is comprised of multiple layers of liquid Argon (LAr) sampler and lead ab-
378 sorber. The choice of its accordion-geometry design brought two main advantages; full
379 ϕ coverage with no non-interactive regions (no cracks); fast extraction of signals coming
380 from both front or rear end of the electrodes. It is made of two half-barrel wheels, both
381 placed in the barrel cryostat, that provide a pseudorapidity coverage up to $|\eta| < 1.475$
382 and two end-cap detectors providing $1.375 \leq |\eta| \leq 3.20$ coverage in two end-cap cryo-
383 stats. The junction between the barrel and end cap components defines the crack region
384 and any signal coming from the crack region is therefore discarded.

385 In the $|\eta| < 1.8$ region there is an additional layer, placed at the front of the calori-
386 meter, that is made of a thin (0.5 cm in the end-cap and 1.1 cm in the barrel) LAr layer
387 with no absorber [17]. This additional layer was designed to correct for the energy lost,
388 as particles enter the calorimeter, by taking a measurement just before the majority of the
389 electromagnetic shower is developed.

390 The Tile calorimeter

391 The main purpose of the hadronic calorimeter is to measure the energy of hadronic
392 showers. It is built employing steel and scintillating tiles coupled to optical fibres which
393 are read out by photo-multipliers. As shown in Figure 2.5, the HCAL is made up of three
394 cylinders; a central barrel, 5.64 m long covering a region $|\eta| < 1.0$, and two extended
395 barrel, 2.91 m long covering a reigon $0.8 < |\eta| < 1.7$. Each cylinder is made up of 64
396 modules and each module is in turn made up of three layers. Ultimately, the smallest

397 section of the calorimeter module is a cell with a $\Delta\phi \times \Delta\eta = 0.1 \times 0.1$ granularity for the
398 two innermost layers and $\Delta\phi \times \Delta\eta = 0.2 \times 0.1$ for the outermost one.

399 2.2.4 The Muon Spectrometer

400 The MS [18], shown in Figure 2.6, is the outermost sub-system of the whole ATLAS de-
401 tector. As such, it surrounds the calorimeters and its main function is to perform precision
402 measurement of muons momenta. The deflection of muon tracks employing large super-
403 conducting air-core toroid magnets and high-precision tracking chambers is at the heart
404 of such high precision measurement.

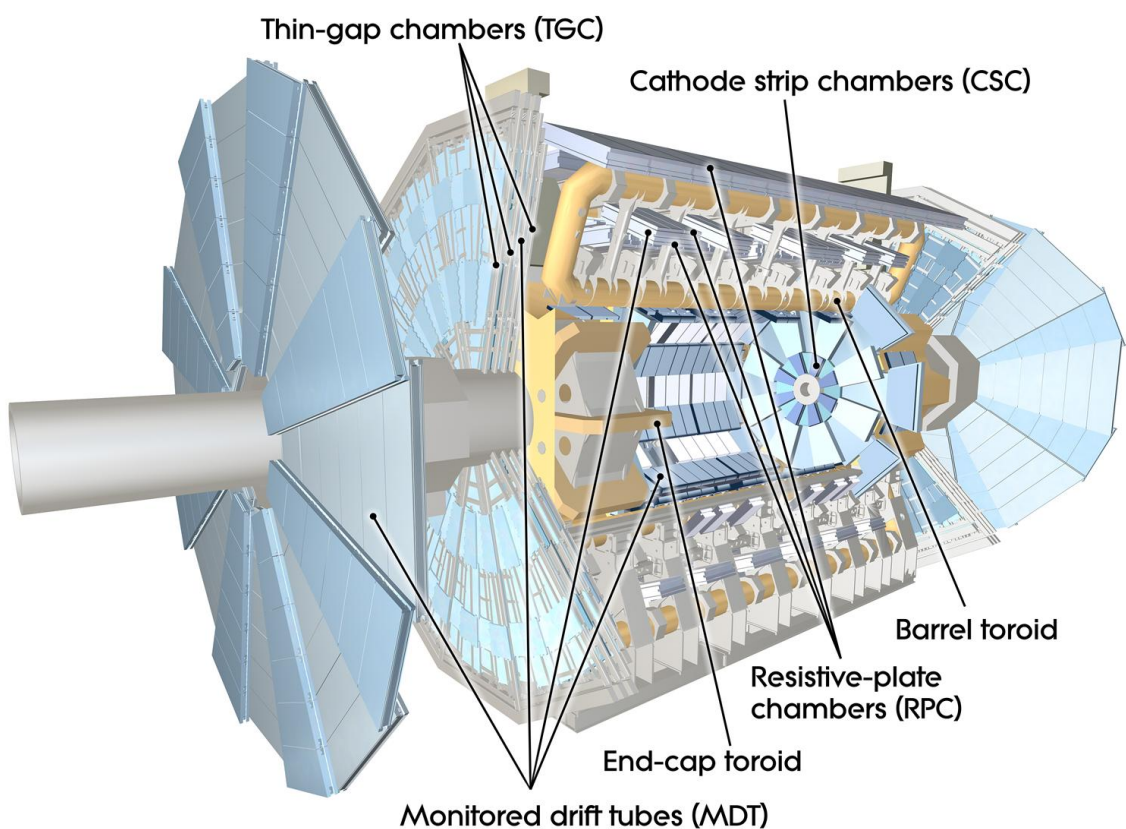


Figure 2.6: Cut-away view of the ATLAS muon system [2].

405 The MS is comprised of one large barrel toroid, covering the region $|\eta| \leq 1.4$, and two
406 end-cap toroids, covering $1.6 < |\eta| \leq 2.7$ which are employed together to achieve the
407 track-bending effect wanted. The magnitude of the magnetic field in the barrel, generated
408 by eight large superconducting coils, ranges from 0.5 to 2 T.

409 Around the beam axis, three cylindrical layers make way for the chambers, placed in
410 planes perpendicular to the beam, used to measure tracks.

411 Monitored Drift Chambers (MDTs) are employed over most of the pseudorapidity

⁴¹² range to provide precision measurement of track coordinates in the bending direction.
⁴¹³ Cathode Strip Chambers (CSCs) are instead employed at large pseudorapidity ($2 < |\eta| <$
⁴¹⁴ 2.7). Finally, in the end-cap regions Thin-Gap Chambers (TGCs) together with Resistive-
⁴¹⁵ Plate Chambers (RPCs) are dedicated to the Trigger System discussed in Section 2.3.

⁴¹⁶ 2.3 The ATLAS Trigger System

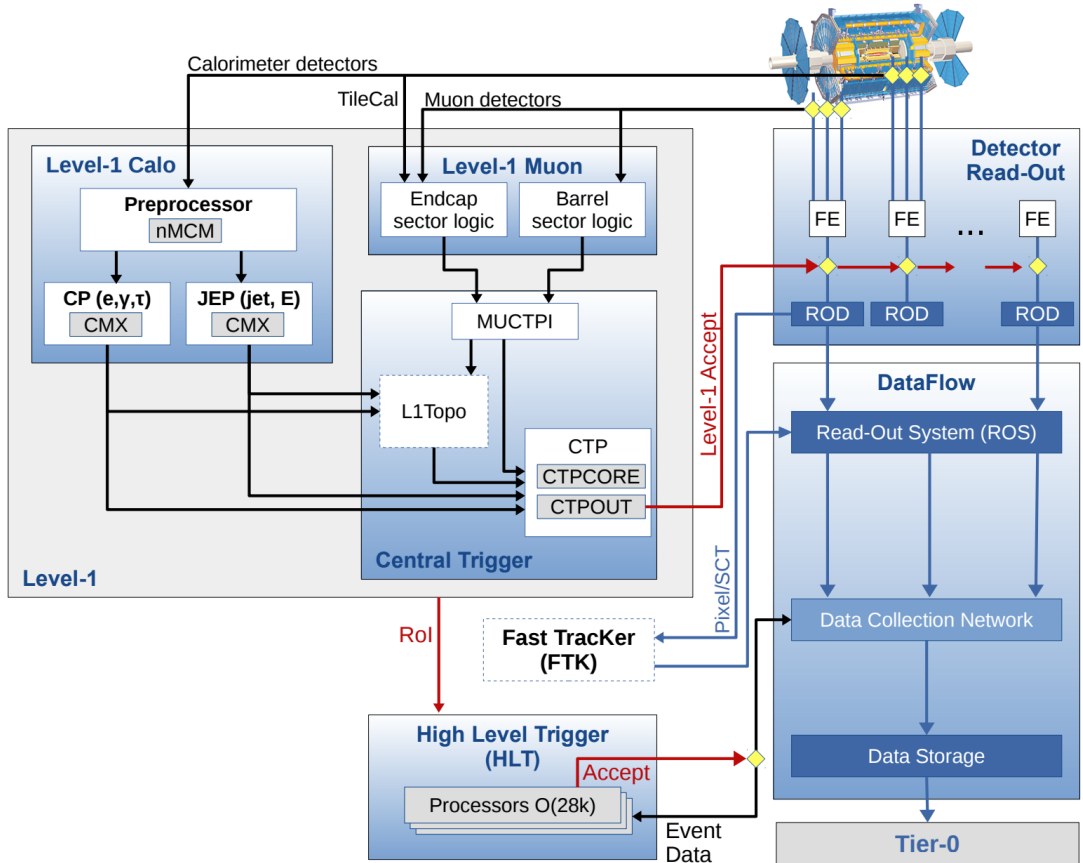


Figure 2.7: The ATLAS TDAQ system. L1Topo and FTK were being commissioned during 2015 and not used for the results shown in this thesis [3].

⁴¹⁷ The ATLAS Trigger System is at the heart of data taking. It is an essential component
⁴¹⁸ of any nuclear or particle physics experiment since it is responsible for deciding whether
⁴¹⁹ or not to store an event for later study [3]. The ATLAS Trigger system is employed to
⁴²⁰ reduce the event rate from ~ 40 MHz¹ bunch-crossing² to ~ 200 Hz which corresponds

¹The LHC delivers beams with a bunch-spacing of 25 ns.

²The term bunch-crossing is hereby used when referring to a collision between two bunches of protons. Since only a certain fraction of the total momentum carried by each proton contributes to the collision, an average number of interactions per bunch-crossing, $\langle \mu \rangle$ is used.

⁴²¹ to roughly 300 MB/s.

⁴²² The Trigger and Data Acquisition (TDAQ) system shown in Figure 2.7 consists of
⁴²³ a hardware-based first level trigger (L1) and a software-based high-level trigger (HLT).
⁴²⁴ The L1 trigger decision is formed by the Central Trigger Processor (CTP), which receives
⁴²⁵ inputs from the L1 calorimeter (L1Calo) and L1 muon (L1Muon) triggers. The first level
⁴²⁶ (L1), which was designed to perform the first selection step, is a hardware-based system
⁴²⁷ that uses information from the calorimeter and muon subdetectors. It also defines the so-
⁴²⁸ called Regions of Interest (RoIs) within the detector to be investigated by the next level
⁴²⁹ trigger, the HLT. Additionally, a Fast TracKer (FTK) system [19] (not yet installed) will
⁴³⁰ provide global ID track reconstruction at the L1 trigger rate using lookup tables stored
⁴³¹ in custom associative memory chips for the pattern recognition. The FPGA-based track
⁴³² fitter will perform a fast linear fit and the tracks are made available to the HLT. This
⁴³³ system will allow the use of tracks at much higher event rates in the HLT than is currently
⁴³⁴ affordable using CPU systems. However, the upgrade of the ATLAS trigger will not be
⁴³⁵ discussed any further.

⁴³⁶ In the next sections the L1 and HLT will be briefly described.

⁴³⁷ 2.3.1 Level 1 Trigger

⁴³⁸ The Level 1 Trigger identifies Regions of Interest (RoIs)³ and passes these to HLT which
⁴³⁹ will perform further investigations. Furthermore, in order to decide whether or not the
⁴⁴⁰ event processing will continue, L1 selection uses only information coming from some
⁴⁴¹ parts of the detector to keep the input rate to a maximum of 100 kHz. L1 is implemented
⁴⁴² in fast custom electronics to keep the latency⁴ below 2.5 μ s. Event data from other sub-
⁴⁴³ syststem are temporarily stored in memories whilst L1 decision is taken.

⁴⁴⁴ The L1 topological trigger (L1-Topo) [20] is feeded with energy and direction inform-
⁴⁴⁵ ation, about the objects found by the L1 calorimeter and the muon trigger, which will be
⁴⁴⁶ processed by dedicated algorithms implemented in its own FPGAs. However, due to the
⁴⁴⁷ 100 kHz read-out rate, not all the information collected by L1-Topo will be sent to the
⁴⁴⁸ HLT, but only part of it. In order to properly seed the ROI-guided HLT reconstruction,
⁴⁴⁹ specific objects in combination with the correct topological criteria must be employed.

³ $\eta - \phi$ regions where event features have been found by the L1 selection process.

⁴Time needed by an electric signal to get to the front-end electronics.

450 2.3.2 High-Level Trigger

451 The HLT is used to reduce the output rate down to 1 kHz and it has a \sim 200 ms average
452 decision time. Events that pass L1 trigger are then processed by the HLT using finer-
453 granularity calorimeter information, precision measurements from the MS and tracking
454 information from the ID. The HLT reconstruction can be run within RoIs identified at L1
455 or a so-called full-scan on the full detector can be performed. The track reconstruction in
456 the Inner Detector is an essential component of the trigger decision in the HLT and it will
457 be discussed more in detail in Chapter 3

458 **Chapter 3**

459 **The b -jet Trigger Signature in ATLAS**

460 The qualification task

461 **3.1 Trigger Efficiency**

462 **Chapter 4**

463 **Event Simulation and Reconstruction**

464 **4.1 Event Generation**

465 **4.1.1 Parton Distribution Functions (PDFs)**

466 **4.1.2 Matrix Element Calculation**

467 **4.1.3 Parton Showers**

468 **4.1.4 Hadronisation**

469 **4.2 Detector Simulation**

470 **4.3 Reconstruction**

471 **4.3.1 Pile-up in the Inner Detector**

472 **4.3.2 Tracks**

473 **4.3.3 Vertex**

474 **4.3.4 Electrons**

475 **4.3.5 Muons**

476 **4.3.6 Jets**

477 **4.3.7 Taus**

478 **4.3.8 Missing Transverse Energy**

479 **4.4 Object Selection**

480 **4.4.1 Baseline Leptons**

481 **4.4.2 Baseline Jets**

⁴⁹¹ **Chapter 5**

⁴⁹² **Stop Searches in all-hadronic final
states**

⁴⁹⁴ **Chapter 6**

⁴⁹⁵ **Results and Statistical Interpretations**

⁴⁹⁶ **Appendix A**

⁴⁹⁷ **Appendix A**

⁴⁹⁸ **Appendix B**

⁴⁹⁹ **Appendix B**

500 Bibliography

- 501 [1] C. Lefèvre, *The CERN accelerator complex.*, <http://cds.cern.ch/record/1260465>.
 502 ix, 7, 8
- 503 [2] ATLAS Collaboration, *The ATLAS experiment at the CERN Large Hadron Collider*,
 504 Journal of Instrumentation **3** no. 08, (2008) S08003.
 505 <http://stacks.iop.org/1748-0221/3/i=08/a=S08003>. ix, 10, 15
- 506 [3] A. Collaboration, *Performance of the ATLAS Trigger System in 2015*, Eur. Phys. J. **C77**
 507 (2017), [arXiv:1611.09661 \[hep-ex\]](https://arxiv.org/abs/1611.09661). ix, 16
- 508 [4] M. Herrero, *The Standard Model.*, <https://arxiv.org/abs/hep-ph/9812242>. 3
- 509 [5] ATLAS Collaboration, *Observation of a New Particle in the Search for the Standard
 510 Model Higgs Boson with the ATLAS Detector at the LHC*, Phys.Lett. **B716** (2012),
 511 [arXiv:1207.7214 \[hep-ex\]](https://arxiv.org/abs/1207.7214). 3
- 512 [6] CMS Collaboration, *Observation of a new boson at a mass of 125 GeV with the CMS
 513 experiment at the LHC*, Phys.Lett. **B716** (2012), [arXiv:1207.7235 \[hep-ex\]](https://arxiv.org/abs/1207.7235). 3
- 514 [7] J.M. Jowett, M. Schaumann, R. Alemany, R. Bruce, M. Giovannozzi, P. Hermes, W.
 515 Hofle, M. Lamont, T. Mertens, S. Redaelli, J. Uythoven, J. Wenninger, *The 2015
 516 Heavy-Ion Run of the LHC*,
 517 <http://accelconf.web.cern.ch/accelconf/ipac2016/papers/tupmw027.pdf>. 6
- 518 [8] O. S. Brüning, P. Collier, P. Lebrun, S. Myers, R. Ostojic, J. Poole and P. Proudlock,
 519 *LHC Design Report.*, <https://cds.cern.ch/record/782076>. 7
- 520 [9] CMS Collaboration, *The CMS experiment at the CERN LHC*, Journal of
 521 Instrumentation **3** no. 08, (2008) S08004.
 522 <http://stacks.iop.org/1748-0221/3/i=08/a=S08004>. 7
- 523 [10] LHCb Collaboration, et. al, *The LHCb Detector at the LHC*, JINST (2008). 7

- 524 [11] ALICE Collaboration, *The ALICE experiment at the CERN LHC*, Journal of
 525 Instrumentation **3** no. 08, (2008) S08002.
 526 <http://stacks.iop.org/1748-0221/3/i=08/a=S08002>. 7
- 527 [12] A. Yamamoto, Y. Makida, R. Ruber, Y. Doi, T. Haruyama, F. Haug, H. ten Kate,
 528 M. Kawai, T. Kondo, Y. Kondo, J. Metselaar, S. Mizumaki, G. Olesen, O. Pavlov,
 529 S. Ravat, E. Sbrissa, K. Tanaka, T. Taylor, and H. Yamaoka, *The ATLAS central*
 530 *solenoid*, Nuclear Instruments and Methods in Physics Research Section A:
 531 Accelerators, Spectrometers, Detectors and Associated Equipment **584** no. 1, (2008)
 532 53 – 74.
 533 <http://www.sciencedirect.com/science/article/pii/S0168900207020414>. 10
- 534 [13] ATLAS Collaboration, *The ATLAS Inner Detector commissioning and calibration*, Eur.
 535 Phys. JC**70**, arXiv:1004.5293. 10
- 536 [14] ATLAS Collaboration, *ATLAS Insertable B-Layer Technical Design Report*,
 537 <https://cds.cern.ch/record/1291633>. 11
- 538 [15] G. A. et al., *ATLAS pixel detector electronics and sensors*, Journal of Instrumentation **3**
 539 no. 07, (2008) P07007. <http://stacks.iop.org/1748-0221/3/i=07/a=P07007>. 12
- 540 [16] A. Bingl, *The ATLAS TRT and its Performance at LHC*, Journal of Physics: Conference
 541 Series **347** no. 1, (2012) 012025.
 542 <http://iopscience.iop.org/article/10.1088/1742-6596/347/1/012025/meta>.
 543 13
- 544 [17] ATLAS Collaboration, *ATLAS liquid-argon calorimeter: Technical Design Report*,
 545 <https://cds.cern.ch/record/331061>. 14
- 546 [18] ATLAS Collaboration, *ATLAS muon spectrometer: Technical design report*,
 547 <https://cds.cern.ch/record/331068>. 15
- 548 [19] ATLAS Collaboration, *Fast TracKer (FTK) Technical Design Report*,
 549 <https://cds.cern.ch/record/1552953>. 17
- 550 [20] E. Simoni, *The Topological Processor for the future ATLAS Level-1 Trigger: from design to*
 551 *commissioning*, arXiv:1406.4316. 17